Volume 1 | Number 1 | Jan 2013 | Pages 1–100

Nanoscale

www.rsc.org/nanoscale

ROYAL SOCIETY OF CHEMISTRY

ROYAL SOCIETY OF CHEMISTRY

www.rsc.org/nanoscale

Journal Name

ARTICLE TYPE

The Role of Domain Size and Titanium Dopant in Nanocrystalline Hematite Thin Films for Water Photolysis[†]

Danhua Yan,[a,b] Jing Tao,[c] Kim Kisslinger,[a] Jiajie Cen,[b] Qiyuan Wu,[b] Alexander Orlov,[b] and Mingzhao Liu[*,a]

Here we develop a novel technique for preparing high quality Ti-doped hematite thin films for photoelectrochemical (PEC) water splitting, through sputtering deposition of metallic iron films from an iron target embedded with titanium (dopant) pellets, followed by a thermal oxidation step that turns the metal films into doped hematite. It is found that the hematite domain size can be tuned from ∼10 nm to over 100 nm by adjusting the sputtering atmosphere from more oxidative to mostly inert. The better crystallinity at larger domain size ensures excellent PEC water splitting performance, leading to record high photocurrent from pure planar hematite thin films on FTO substrates. Titanium doping further enhances the PEC performance of hematite photoanodes. The photocurrent is improved by 50%, with a titanium dopant concentration as low as 0.5 atom%. It is also found that the role of titanium dopant in improving the PEC performance is not apparently related to the films' electrical conductivity which had been widely believed, but is more likely due to the passivation of surface defects by the titanium dopants.

INTRODUCTION

Driven by a strong desire for clean and renewable fuel, effective methods of hydrogen (H_2) production have been sought after for a long time. Solar water splitting within a photoelectrochemical (PEC) cell has been one of the most promising methods since 1972, when Fujishima and Honda first reported electrochemical photolysis of water using a TiO_2 electrode under UV radiation.[1] The key component of a PEC cell, the semiconductor photoelectrode, is responsible for carriers generation through light absorption, which initiates redox reactions in water to produce hydrogen and oxygen.[2] Continuous efforts of finding suitable semiconductor materials for photoelectrodes are being made to further improve the PEC cell performance.[3] α-Fe_2O_3, or hematite, becomes attractive for its vast abundance in the earth's crust, low cost, and stability in both the atmosphere and water, together with a suit-

able band gap (2.0 eV, corresponding to $\lambda = 620$ nm) to optimize the harvest of visible sunlight.[4] However, both the photocurrent density and the photocurrent onset of hematite photoelectrodes are far short of the theoretical expectation, due to the poor electrical conductivity, high carriers recombination rate,[5–7] and slow kinetics of water redox reactions.[4,8,9] It has been widely studied to modify hematite through morphology controls and chemical modification, among which doping is particularly promising.

Hematite can be doped as an *n*-type semiconductor with dopants such as titanium, silicon, tin, and platinum, which may help improve its electrical conductivity and photocatalytic activities.[10–14] In the case of titanium, a variety of techniques, including spray pyrolysis,[15–17] atmospheric pressure chemical vapor deposition (APCVD),[5,13] hydrothermal synthesis,[18,19] and electrodeposition[20] have been employed to prepare doped hematite photoelectrodes. Various groups have attributed the improved performance of Ti-doped hematite to an increase in majority carrier (electron) density,[21,22] improved crystallinity[21], or enhancement of electron transport within bulk hematite and decrease of surface recombination.[23] However no conclusive consensus has been reached regarding the dopant's exact role. The difficulty is partially due to the unintentionally changes in the morphology and surface structures when impurities (dopants) are incorporated, which introduces additional uncertainty for analyzing the doping effects.[13,24–26] It is therefore highly desirable for a method that produces doped thin films in a consistent manner

[a] Center for Functional Nanomaterials, Brookhaven National Laboratory, Upton, New York 11973, United States; E-mail: mzliu@bnl.gov
[b] Department of Materials Science and Engineering, Stony Brook University, Stony Brook, New York 11794, United States
[c] Condensed Matter Physics and Materials Science Department, Brookhaven National Laboratory, Upton, New York 11973, United States

[†] Electronic Supplementary Information (ESI) available: ESI contains details about the dependence of PEC activity on sample thicknesses, thermodynamic calculation for reactions between FTO and elemental titanium/iron, and model of Mott-Schottky analysis and measurement of depletion region capacitance. See DOI: 10.1039/b000000x/

that is independent of dopant type or concentration. Limited efforts have been made to produce uniformly doped hematite thin films, employing techniques such as atomic layer deposition (ALD),[27–30] pulsed laser deposition (PLD),[31] and reactive magnetron sputtering[10]. However, these techniques suffer from little flexibility in dopant species or concentrations. ALD requires specific organometallic precursors for each dopants, while PLD and traditional magnetron sputter both require alloyed targets, in which the dopant species and concentrations are fixed.
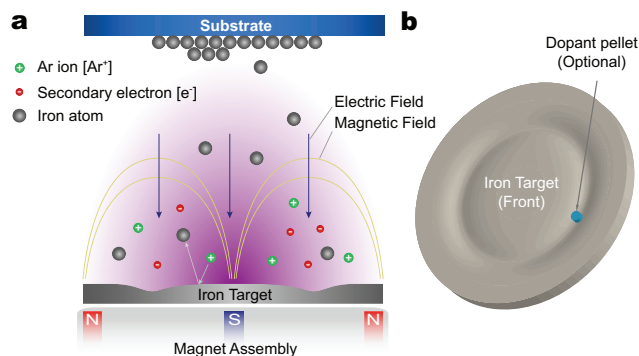
Fig. 1 (a) Magnetron sputtering is used to deposit iron thin films, as the precursor for the hematite films. (b) For doping application the iron sputtering target is drilled for embedment of dopant pellet(s). The circular indentation on the iron target surface corresponds to the area of the highest Ar$^+$ plasma density.

Here we report a modified magnetron sputtering deposition technique to produce uniform hematite thin films, in which the dopants species and concentrations could be readily adjusted. Considered an ideal method to produce higher quality thin films,[32] magnetron sputtering follows a basic working principle illustrated in Figure 1a. The target is mounted over a permanent magnets assembly, around which a strong electrical field (DC or RF) ionizes the argon atmosphere into a plasma of Ar$^+$ ions and electrons. The Ar$^+$ ions then bombard against the target surface, which subsequently ejects target atoms. Plasma density close to the target is strongly influenced by the magnetic field, leading to higher sputtering rate at an annular ring over the target. For doping application we drill one or more small holes at this annular ring for embedment of dopant pellet(s) (Figure 1b). The dopants can be easily alternated with different metal pellets, and the doping level can be controlled by the number and the size of the pellets. In this case we use a pure iron target that is embedded with titanium pellet(s). Unlike methods that deposit Fe$_2$O$_3$ directly, we apply a "deposition – oxidation" strategy, in which pure or titanium-doped iron films are first deposited at room temperature and are subsequently annealed in oxygen at higher temperature to form hematite films (Scheme 1). The two-step process not only provides well controlled doping level but also improves quality of hematite films when compared to single step methods.[10,33,34] In this work we optimize the PEC water splitting activity of these hematite films through a systematic study of critical deposition parameters including the titanium concentration, the sputtering atmosphere, and the film thickness. We find that titanium doping significantly improves the film's water splitting activity, even at a

very low dopant concentration (0.5 atom%). On the other hand, we note that the grain size and photocatalytic performance of the Ti-doped hematite thin films can be readily tuned by varying the sputtering atmosphere from inert to mildly oxidative, which is achieved by mixing a certain fraction of oxygen to the argon carrier gas. In addition, we find that the hematite film's electrical conductivity is not increased but decreased at low concentration of titanium doping, suggesting that its role may not be as simple as proposed in earlier studies.
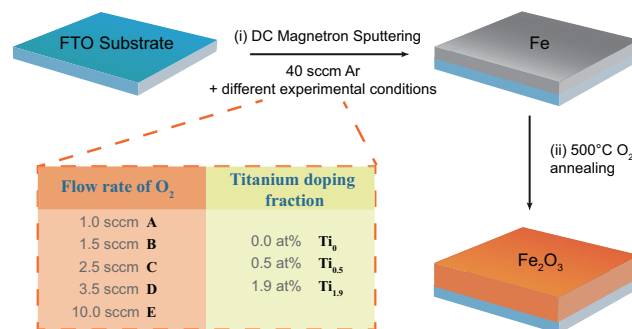

Scheme 1 The two-step "deposition – oxidation" technique for hematite thin films fabrication involves (i) the deposition of iron thin films under various conditions and (ii) their thermal oxidation under a fixed condition. The samples are named accordingly, e.g., a sample deposited under a flow of 40 sccm Ar (always fixed) and 1.0 sccm O$_2$, with a titanium doping of 0.5 atom%, is named Sample **ATi**$_{0.5}$.

RESULTS AND DISCUSSION

In Scheme 1 we list the deposition parameters used for hematite thin film synthesis, including sputtering condition and titanium doping concentration, and introduce the naming rule for the samples. Pure or titanium doped iron metal films are first sputtered over various substrates such as fluorine-doped tin oxide (FTO) glasses or silicon wafers, and all samples in the following discussions are deposited to a thickness of 25 nm, monitored *in situ* by a quartz crystal microbalance (QCM), which provides better PEC performance than any other thicknesses in our method (Supporting Information, Figure S1). A thermal oxidation process at 500°C is followed to convert iron into hematite. The phase diagram of iron oxides does indicate that hematite is the single most stable phase in pure O$_2$ at 500°C.[35]

To better investigate the doping conditions and crystallinity of Ti-doped hematite thin films, samples are first deposited over silicon wafers to eliminate undesired background signal. X-ray diffraction (XRD) confirms the rhombohedral lattice structures of Ti-doped hematite thin films (Figure 2a). Diffraction peaks are indexed using a standard pattern from synthetic hematite (JCPDS#33-0664). Across all the samples we find that the strongest hematite diffraction signal is always from the (104) plane, indicating it as the preferred orientation for the films. The annular-integrated selective area electron diffraction (SAED) pattern (Figure 2a, *inset*) further confirms the formation of hematite after thermal oxidation. The apparent difference in peak intensities of XRD and integrated SAED patterns is due to their very different incident beam orientation. The presence of titanium

in hematite films is confirmed by energy dispersive X-ray spectroscopy (EDX, Figure 2b). A dopant concentration as low as 0.5 atom% is achieved by embedding one single cylindrical titanium pellet to the iron sputtering target. By embedding more titanium pellets the total exposed surface area of titanium is increased, leading to higher doping concentration. X-ray photoelectron spectroscopy (XPS) finds the valence state of titanium in hematite films to be 4+, and confirms the dopant concentration given by the EDX measurement (Supporting Information, Figure S2).
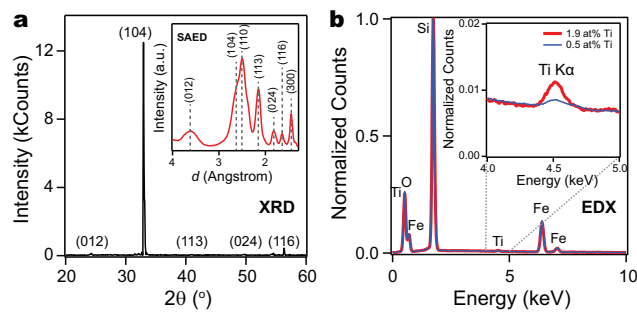
Fig. 2 (a) XRD patterns of a Ti-doped hematite thin film deposited on silicon wafer(Sample **ATi**$_{0.5}$). (*inset*) Integrated selective-area electron diffraction pattern for Sample **ATi**$_{0.5}$. (b) EDX spectra of Samples **ATi**$_{0.5}$ and **ATi**$_{1.9}$, which are both deposited on silicon wafers. The counts are normalized by the silicon Kα line.

Pure or Ti-doped hematite are deposited onto conductive FTO glasses substrates to produce water splitting photoelectrodes. When deposited over FTO substrate in pure argon atmosphere, iron thin film sputtered from both pure and Ti-embedded iron target features metallic smooth finish (Supporting Information, Figure S3a). Although pure iron thin films are converted to uniform orange colored films after rapid thermal annealing (RTA) in O$_2$, as expected for hematite (Supporting Information, Figure S3b),[10,30] the Ti-doped thin films appear very uneven in color after the same process (Figure 3a), which is likely due to the chemical reaction between elemental titanium and the FTO substrates during the heating. Thermodynamic calculation indicates that it is highly favorable for elemental titanium to reduce tin oxide to elemental tin both at room temperature and at 500°C, but not favorable for elemental iron to do so (Supporting Information). Moreover, with a melting point of just 232°C, elemental tin can readily diffuse into the hematite layer during annealing at 500°C, which is visualized by cross-sectional EDX mapping (Figure 3c). The diffusion of elemental tin also interferes with the crystallization of hematite, leaving significant inhomogeneity and porosity across the specimen, as shown by the cross-sectional scanning TEM image (Figure 3b). The decrease in thickness of FTO layer (from ~300 nm to ~285 nm) is consistent with the diffusion of tin from the substrate to hematite.

The undesired reaction between titanium and FTO can be inhibited by the introduction of a minimal flow of O$_2$ during the sputtering deposition. Even when the introduced O$_2$ is insufficient to completely oxidize the deposited film, as it remains its metallic appearance, the film nevertheless turns uniformly orange after its complete RTA oxidation (Figure 3d). The formation of
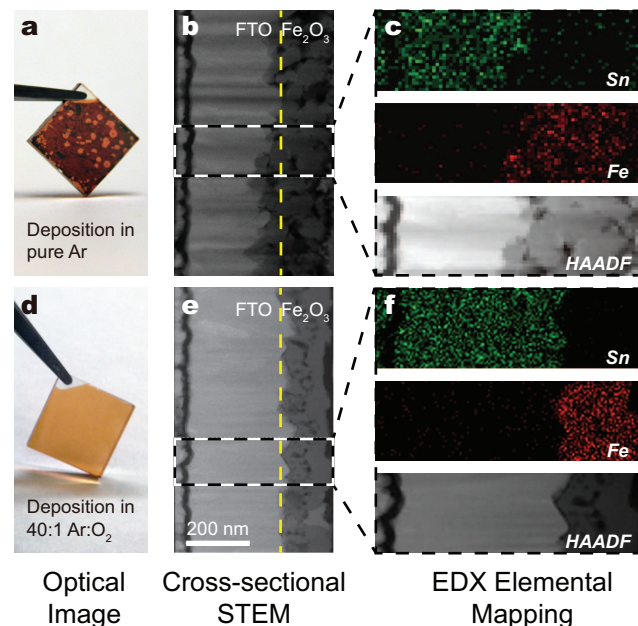
Fig. 3 (a) After the oxidative annealing, Ti-doped iron film deposited in pure argon over an FTO substrate appears very uneven in color. The FTO/hematite boundary is blurred (b) as evident by the cross-sectional STEM image, with (c) tin diffused into the hematite layer according to the EDX mapping. (d) The inhomogeneity disappears when the Ti-doped iron film is deposited in an atmosphere of 40:1 Ar:O$_2$ mixture, with (e) a sharper FTO/hematite boundary and (f) negligible diffusion of tin into hematite.

hematite over FTO glasses is confirmed by XRD (Supporting Information, Figure S4).The substrate layer and the hematite layer are clearly divided as the diffusion of tin is prevented effectively (Figure 3e, 3f). Besides inhibiting the undesired reaction, we find that the amount of oxygen introduced during the sputtering deposition has a profound impact on the structure (Figure 4) and the photocatalytic performance of the hematite thin film electrodes eventually made. By fixing the argon flow to 40 sccm, the iron thin films are deposited to a same thickness with different flow rates of O$_2$ (1–10 sccm), and are subsequently fully oxidized to hematite under an identical RTA condition (Scheme 1). The morphology variation brought by different sputtering atmosphere is clearly shown by SEM images presented in Figure 4a and TEM images presented in Figure 4b. Produced with 1.0 sccm O$_2$ flow (Sample **ATi**$_{0.5}$), the Ti-doped hematite thin film appears highly textured, with domain size over 100 nm. With 1.5 sccm O$_2$ flow (Sample **BTi**$_{0.5}$), the textured structure becomes sparse with smaller grains developing beneath. Samples produced with 2.5 sccm (Sample **CTi**$_{0.5}$), 3.5 sccm (Sample **DTi**$_{0.5}$) and 10 sccm O$_2$ flows (Sample **ETi**$_{0.5}$) appear very flat with uniformly distributed grains as tiny as ~10 nm. The evolution of morphology is clearly correlated to the thin films' degree of oxidation during their sputtering deposition. The highly textured structures produced at low O$_2$ flow is due to the dramatic expansion of metal lattices during the RTA oxidation at 500°C, as oxygen atoms enters the lattices. When oxidized from iron to hematite, the thin film expands by about two folds in volume. In contrast, deposition under higher O$_2$ flows oxidizes most of the iron atoms into hematite clusters
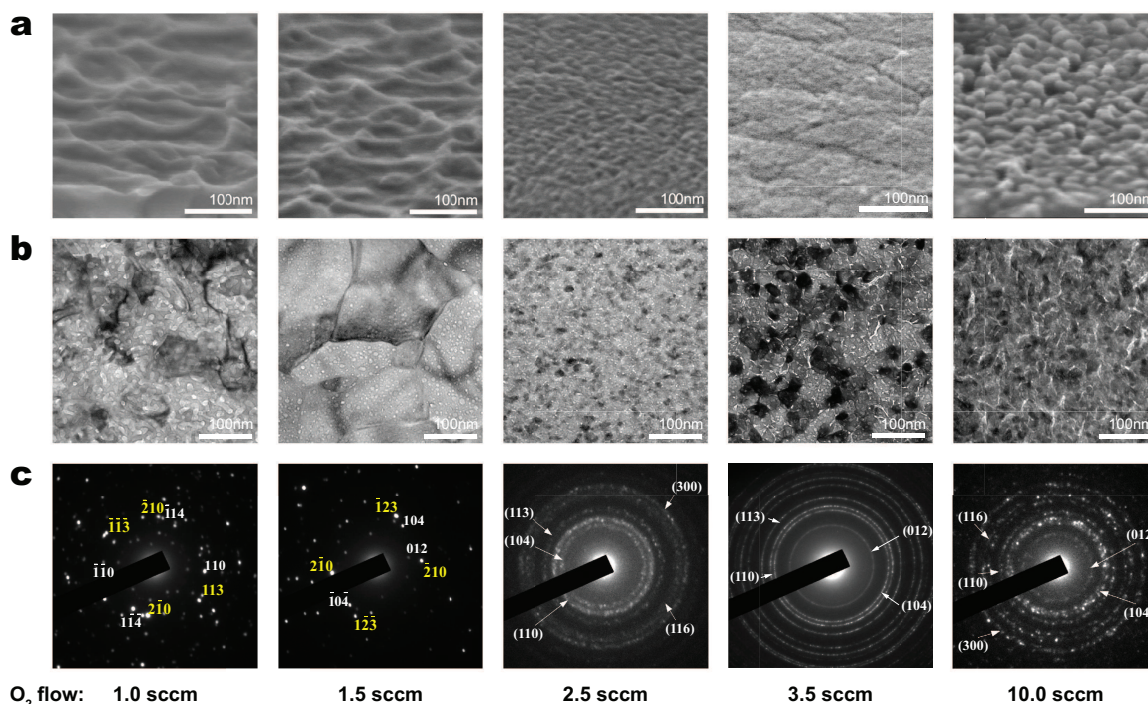
Fig. 4 The morphology and domain sizes of Ti-doped hematite films are strongly affected by the O_2 flow rate (1.0 sccm, 1.5 sccm, 2.5 sccm, 3.5 sccm and 10.0 sccm) used during the sputtering deposition of iron films, according to their (a) SEM images (20° tilted), (b) TEM images, and (c) SAED patterns.

in situ, meaning that the volume expansion during the final RTA oxidation is minimal. SAED patterns clearly demonstrate the variation of grain sizes between different samples (Figure 4c). All the diffraction patterns are collected over an area of same size. Samples deposited under higher flows of O_2 (Sample $CTi_{0.5}$, Sample $DTi_{0.5}$ and Sample $ETi_{0.5}$) give diffraction patterns of concentric rings, indicating a highly polycrystalline structure in these samples. On the other hand, samples deposited under lower flows of O_2 (Sample $ATi_{0.5}$ and Sample $BTi_{0.5}$) give diffraction patterns of isolated spots, which can be indexed into a small number of groups with different crystal orientations, suggesting larger crystal domains and better crystallinity. It is therefore apparent that a hematite thin film of large domain size is formed when the majority of iron is oxidized during the second step of 500°C RTA, rather than being oxidized *in situ* during the first step of sputtering deposition. On the contrary, the tiny Fe_2O_3 clusters formed during the sputtering deposition with 2.5 sccm or higher O_2 flow do not grow further during the RTA oxidation. The finding is consistent with literature reports that indicate the annealing of hematite at ∼500°C have no significant impacts on its crystal domain size and structure.[36–38] The trend of decreasing domain size is reversed toward the highest O_2 flow of 10 sccm (Sample $ETi_{0.5}$), which shows slightly larger grains. However, the film is now becoming significantly more porous with large gaps between domains (Supporting Information, Figure S5).

Such significant difference in crystallization will no doubt impact on their photocatalytic performances. Indeed, the hematite photoelectrodes prepared with different O_2 flows during sputtering deposition behave rather differently for PEC measurements (Figure 5a). It is clearly seen that Sample $ATi_{0.5}$ presents the highest photocurrent density, 0.415 mA·cm^{-2}, at the thermodynamic potential of oxygen evolving (1.23 V_{RHE} at 25°C) under AM 1.5 G illumination, and that the onset potential for anodic current is at ∼1.0 V_{RHE}. A decrease in photoelectrochemical performance follows the increase in O_2 flow during sputtering deposition, e.g., Sample $ETi_{0.5}$ generates merely ∼0.003 mA·cm^{-2} at 1.23 V_{RHE}, with onset potential shifting ∼0.1 V more anodic. Such drastically drop in photocurrents can be also observed in 1.9 atom% Ti-doped samples (Supporting Information, Figure S6). These results are well correlated to the microscopic structure of these thin films, that the smaller grain sizes of higher O_2 flow samples lead to significant increase of grain boundaries and surface defects,[39,40] which effectively trap photo-generated electrons and holes, thus promoting carrier recombination in the thin films. As the photocurrent is primary limited by the carrier recombination processes,[41] the trend in the PEC activity agrees well with the changes in grain size.

The dopant concentration is further investigated to better understand the role of titanium doping, by varying the numbers of titanium pellets being embedded. As shown in Figure 5b, titanium doping at 0.5 atom% increases the photocurrent by ∼50% when compared to pure hematite thin film produced under identical conditions, from 0.277 mA·cm^{-2} to 0.415 mA·cm^{-2} at 1.23 V_{RHE}. Although previous reports usually involve higher level of titanium doping (2% ∼ 5%),[9,10,19,20,23,30,42] we find a very small concentration (∼0.5 atom%) of titanium already
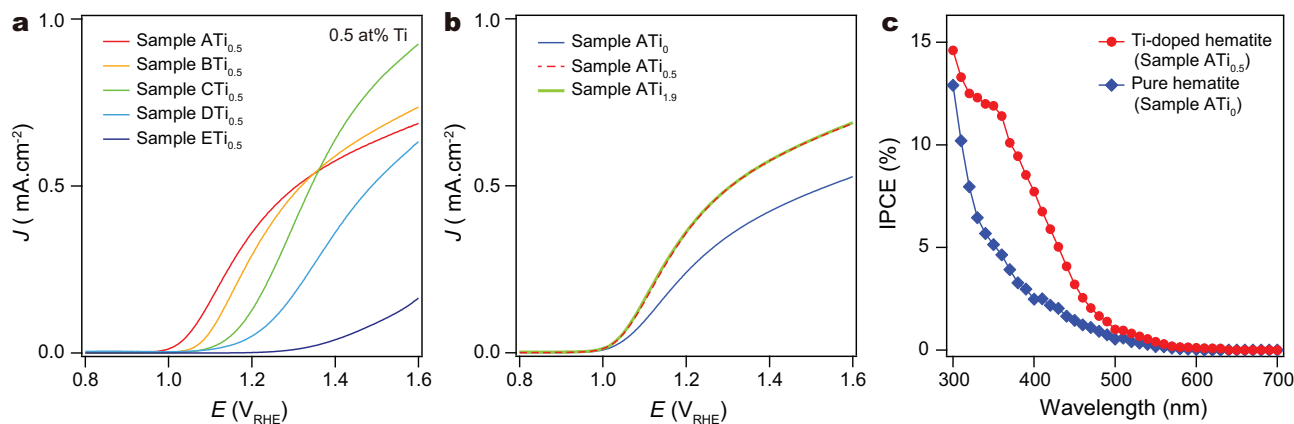
Fig. 5 Current density *vs.* potential curves under AM 1.5 G illumination for various hematite thin films: (a) 0.5 atom% Ti-doped films prepared with different O_2 flow rate during sputtering deposition; (b) films deposited under 1 sccm O_2 with different Ti-doping level. (c) IPCE is plot against incident wavelength for undoped and Ti-doped hematite thin films at 1.46 V_{RHE}.

has significant effect for improving the photocatalytic activity. In fact, samples doped with higher concentration of titanium ($\sim$1.9 atom%) shows no additional improvement, indicating only a small amount of Ti doping is needed for the improvement. It is worth noting that a doping concentration of 0.5 atom% is equivalent to a titanium density of $2 \times 10^{20}\,\text{cm}^{-3}$ in hematite, which is already a very high dopant concentration from the perspective of semiconductor physics. On the other hand, photocurrent from our pure hematite film ($0.277\,\text{mA·cm}^{-2}$) remains higher than previous results on planar hematite thin film electrode prepared by other techniques, including the reactive DC magnetron sputtering method.[10,30] The improvement likely attributes to our two-step "deposition – oxidation" technique, which provides better crystallinity of hematite film electrodes through the RTA oxidation of iron thin films.

Further details of PEC performance are studied by measuring the incident photon-to-current efficiency (IPCE), which is the ratio of the number of photo-generated electrons to the number of incident photons (Figure 5c). The measurements are performed at 1.46 V_{RHE} with incident wavelength in the 300$\sim$700 nm range. It is clearly shown that the titanium doping improves the overall IPCE of hematite thin films at wavelength shorter than 480 nm. The improvement is most significant around 350 nm, where the IPCE is more than doubled through the titanium doping. The relatively low IPCE beyond 480 nm (2.58 eV) is consistent with hematite being an indirect band gap semiconductor, as indirect transition is usually associated with much weaker light absorption. By analyzing the optical absorption spectrum of our hematite sample we find its direct band gap at $\sim$2.57 eV (482 nm) and indirect band gap at $\sim$1.77 eV (700 nm), which agrees with previous reports (Supporting Information, Figure S7).[33,43] The result thus confirms that the higher efficiency observed at $\lambda < 480$ nm is due to the excitation of the direct band gap.

Electronic properties of undoped and Ti-doped hematite thin films, including the flat band potential (E_{fb}) and donor density (N_D), are obtained from the Mott-Schottky analysis. The space charge capacitance C_0 is determined by electrochemical impedance spectroscopy (EIS) measurements performed at 1 kHz
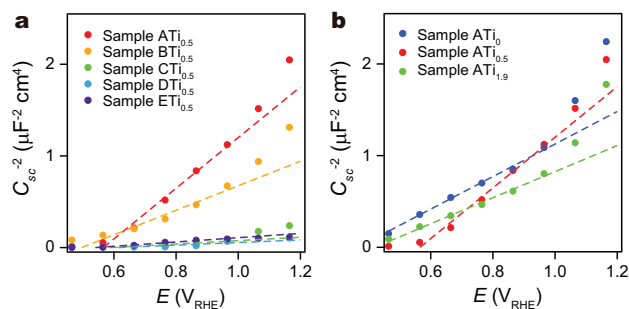
Fig. 6 Mott-Schottky plots for (a) Ti-doped hematite thin films with different O_2 flow rate during sputtering deposition and (b) hematite thin films deposited under 1 sccm O_2 with different Ti-doping level. Dash lines are linear fits for corresponding data at $E < 1.0$ V_{RHE}.

and is normalized by the surface area $A = 1\,\text{cm}^2$ in our case (Supporting Information). For a planar semiconductor|electrolyte interface, capacitance and applied potential follow the Mott-Schottky equation:

$$\frac{1}{C_{SC}^2} = \frac{A^2}{C_0^2} = \frac{2}{e\varepsilon\varepsilon_0 N_D}\left(-\Delta\phi - \frac{k_B T}{e}\right) \qquad (1)$$

where e is the elementary charge, ε the semiconductor dielectric constant ($\sim$20 for hematite), ε_0 the vacuum permittivity, $\Delta\phi = E - E_{fb}$ the magnitude of band bending at the semiconductor|electrolyte interface, and $k_B T$ the thermal energy. All the samples measured present a linear relationship between $1/C_{SC}^2$ and E within lower potential range (< 1.0 V_{RHE}) (Figure 6). Positive slopes of these samples indicate that all the hematite thin films are *n*-type. Linear fitting of $1/C_{SC}^2$ *vs.* E gives N_D and E_{fb} according to Eq. (1). The results are summarized in Table 1 and Table 2.

Mott-Schottky plots of hematite thin films with different titanium doping concentration are shown in Figure 6b, with the flat band potential (E_{fb}) and donor density (N_D) derived from these plots summarized in Table 2. The donor density of 0.5 atom% Ti-doped Sample **ATi$_{0.5}$** ($N_D = 2.6 \times 10^{18}\,\text{cm}^{-3}$) is surprisingly lower than the pure hematite Sample **ATi$_0$** ($N_D = 4.0 \times 10^{18}\,\text{cm}^{-3}$). Only

Table 1 Electrical Properties of Ti-doped hematite thin films (0.5 atom% Ti doping, with different O_2 flow during sputtering deposition).

| O_2 flow (sccm)	N_D (cm^{-3})	E_{fb} (V$_{RHE}$)
1.0	$2.55 \pm 0.16 \times 10^{18}$	0.54 ± 0.01
1.5	$5.27 \pm 0.71 \times 10^{18}$	0.47 ± 0.04
2.5	$3.82 \pm 1.50 \times 10^{19}$	0.56 ± 0.07
3.5	$4.95 \pm 2.99 \times 10^{19}$	0.59 ± 0.10
10.0	$3.01 \pm 0.26 \times 10^{19}$	0.51 ± 0.02

Table 2 Electrical Properties of pure or Ti-doped hematite thin films (1.0 sccm O_2 flow during sputtering deposition, with different Ti-dopant concentration c_{Ti}).

c_{Ti} (atom%)	N_D (cm^{-3})	E_{fb} (V$_{RHE}$)	ρ ($\Omega \cdot$m)	σ (S$\cdot$m^{-1})
0	$3.97 \pm 0.18 \times 10^{18}$	0.34 ± 0.02	$0.94 \pm 0.13 \times 10^2$	$1.06 \pm 0.17 \times 10^{-2}$
0.5	$2.55 \pm 0.16 \times 10^{18}$	0.54 ± 0.01	$3.73 \pm 0.73 \times 10^2$	$2.68 \pm 0.41 \times 10^{-3}$
1.9	$4.96 \pm 0.31 \times 10^{18}$	0.39 ± 0.02	$1.33 \pm 0.35 \times 10^2$	$7.52 \pm 2.53 \times 10^{-3}$

at higher titanium doping concentration (1.9 atom%) does the donor density increase to 5.0×10^{18} cm^{-3}. This trend is consistent to the results from conductivity measurements (Table 2), i.e., the conductivity first decreases when a low concentration (0.5 atom%) of titanium is doped to pure hematite but increases at higher doping. The results suggest that although the doping of titanium clearly improves the PEC activity of hematite, the improvements are not apparently related to the enhanced conductivity as suggested before,[44] that is, the role of titanium is not as simple and naïve as an n-type donor. In fact, considering that the voltage drops across such a thin Ti-doped hematite film ($\sim$70 nm for our samples, Supporting Information) is merely about 1 mV at a current density of 1 mA$\cdot$cm^{-2}, it is not surprising that the films' electrical conductivity has little effect on their photocatalytic activity in our case.

According to Figure 6a and Table 1, it is clear that N_D increases for samples deposited under higher O_2 flow, while the flat band potential remain constant at 0.53 ± 0.06 V$_{RHE}$. Donor density (N_D) of n-type semiconductors at room temperature reflects the concentration of positively charged impurities in intrinsic semiconductors,[45] where the impurities are mainly made of dopants and defects in materials. That is, N_D measured from Mott-Schottky plot is the total donor concentration, which may or may not ionize to make free carriers. As titanium dopant concentrations are fixed in these samples and all the samples are oxidized completely under an identical RTA condition, the increasing of N_D with increased O_2 flow is likely the outcome of higher concentration of defects in hematite thin films due to the decreased domain sizes.

It is worth noting that the titanium doping may affect not only the *bulk* of hematite but also its surface, that the presence of titanium on the surface of hematite is inevitable due to the uniform distribution of titanium dopants in hematite. To better understand the surface effect of titanium doping, we simulate the surface condition of Ti-doped hematite thin films by intentionally depositing only a small amount of TiO_2 over pure hematite (Sample **ATi$_0$**) using atomic layer deposition (ALD). The deposition thickness is well controlled by the ALD purging cycles to ensure that the hematite surface is not fully covered by TiO_2. The procedure we follow deposits one full monolayer (ML) of TiO_2 per 10 cycles. A TiO_2 deposition of merely 2 cycles (0.2 ML) does significant improve the photocurrent and the onset potential (Figure 7a).
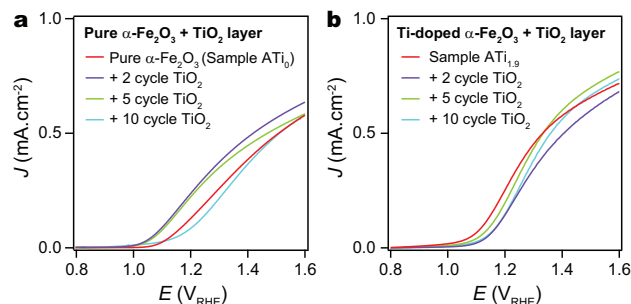
Fig. 7 Photocurrent density vs. potential curves of (a) pure hematite (Sample **ATi$_0$**) coated with an ALD TiO_2 layer of various thickness and (b) Ti-doped hematite (Sample **ATi$_{1.9}$**) coated with an ALD TiO_2 layer of various thickness.

Correspondingly the IPCE is also improved by the TiO_2 sub-monolayer over the hematite surface (Supporting Information, Figure S9). The improvement is not due to the negligible light absorption of TiO_2. In fact, PEC performance decreases for samples coated with 5 or 10 cycles of TiO_2, as a thicker TiO_2 layer blocks the minority carrier (hole) transportation due to its deeper valence band edge. Since such a small amount of TiO_2 on surface neither changes the conductivity nor the morphology of the hematite films, the enhancement of PEC performance is clearly due to the passivation of the surface states of hematite electrode by titanium.[29,44] We therefore propose that the improvement due to Ti-doping in hematite may be largely attributed to the inevitable presence of titanium atoms at hematite surface, which may either passivate the surface defects or provide better catalytic centers for oxygen evolving. To test this hypothesis, we deposit TiO_2 over Ti-doped hematite (Sample **ATi$_{1.9}$**) for comparison. It turns out that the additional TiO_2 coating on the surface no longer enhances the PEC performances (Figure 7b), in sharp contrast to the pure hematite electrode. The result implies that the Ti-doped hematite electrode already has sufficient titanium at its surface to passivate the defects so that additional TiO_2 deposited to the surfaces no longer improves its photocatalytic activity.

CONCLUSIONS

In summary, the modified magnetron sputtering deposition technique we develop provides a novel route for preparing higher

quality hematite thin films with the capability to incorporate different doping elements with tunable doping level. A two-step "deposition – oxidation" technique is adopted for better crystallinity it provides, which leads to record high photocurrent from planar pure hematite thin films. Introducing a controlled small stream of O_2 during the sputtering deposition not only inhibits the undesired chemical reaction between substrates and the titanium dopants, but also influences the crystallinity of the hematite film. The largest hematite domain size is achieved by limiting O_2 flow during the sputtering deposition as low as possible. When deposited at the optimal condition, Ti-doping significant increases the photocurrent generated from hematite thin film photoanodes, at a doping concentration as low as ∼0.5 atom%. We find that the exact role of titanium dopant for improving the photocatalytic activity is not apparently related to the films' electrical conductivity which had been widely believed, but is more likely due to the passivation of hematite surface defects by the titanium dopants. The strategy of preparing undoped or doped hematite thin films we present here can be readily applied to various doping species and concentration by modifying dopant pellets, and should be promising in further understand of doping effects in hematite for PEC water splitting.

METHODS

Preparation and characterization of doped/undoped hematite thin films.

Pristine or Ti-doped iron thin films are deposited over fluorine-doped tin oxide (FTO) coated glasses (MTI Corporation, 12∼14 Ω/sq) or silicon wafers (<100> orientation, 300 nm thermal oxide) by magnetron sputtering, in a Lesker PVD 75 physical vapor deposition system. All the substrates are cleaned in oxygen plasma prior to deposition process. For pure iron films we use iron plate (99.9+% purity) as the sputtering target and for Ti-doped ones we embed cylindrical titanium pellets (99.995% purity, 1/8" diameter × 1/8" height) to the iron plate. The magnetron sputtering is held under argon flow of 40 sccm and various flow rates of oxygen. The deposition is conducted with the substrates held at room temperature until a desired thickness is reached, per reading from an *in situ* quartz crystal microbalance (QCM). After the deposition, iron thin films are heated in oxygen at 500°C for 10 minutes in a rapid thermal annealer (RTA), to fully oxidize the iron films to hematite thin films. X-ray diffraction (XRD, Rigaku Ultima III) is conducted to confirm the formation of hematite. The presence of titanium in hematite films is confirmed by energy-dispersive X-ray spectroscopy (EDX, JEOL 7600F). K-line intensities are used for both iron and titanium quantifications, and the standard intensities used for calculation are directly from INCA Energy software database. X-ray photoelectron spectroscopy (XPS, RHK Technology UHV 7500) is conducted to further confirm the existence and valence of titanium dopant. For XPS quantification and calibration, the sensitivity factors we adopted are from Wagner empirically database. Scanning electron microscopy (SEM, Hitachi S4800) and transmission electron microscopy (TEM, JEOL 1400) respectively reveal the morphology and crystal structures of the thin films prepared with different parameters. Cross sectional specimens of selected thin film samples are prepared by focused ion beam milling (FEI HELIOS 600), from which high angle annular dark-field (HAADF) and EDX mapping images are collected simultaneously by a JEOL ARM-200F TEM. For studying the role of titanium doping, ultra-thin TiO_2 is deposited over pure hematite films by atomic layer deposition (ALD, Savannah S100, Cambridge Nanotech) at 150°C for various cycles (growth rate ∼0.02 nm/cycle).

Electrochemistry and photoelectrochemistry (PEC) measurements.

The photocatalytic performance of pure and Ti-doped hematite films on FTO substrates are measured by a potentiostat (VersaStat4, PAR), using a three-electrode PEC cell under illumination of a 150 W solar simulator with an AM 1.5 G filter (Newport). The hematite thin film coated FTO substrate is used as the working electrode with an active illumination area of 1.0 cm^2, with a platinum wire as the counter electrode, an Ag|AgCl|3 M KCl electrode as the reference electrode (0.1941 V_{NHE} at 25°C), and a 0.1 M KOH solution (pH = 13) solution as the electrolyte. The potential recorded experimentally, $E_{AgCl/Ag}$, is converted to a potential in reference of the reversible hydrogen electrode (RHE), E_{RHE}, according to the Nernst equation:

$$E_{RHE} = E_{AgCl/Ag} + E^{\circ}_{AgCl/Ag} + 0.05917\text{pH} \tag{2}$$

where the E_{RHE} is the potential converted, $E_{AgCl/Ag}$ is the potential measured, $E^{\circ}_{AgCl/Ag} = 0.1941$ V_{NHE} at 25 °C, and pH = 13 in our case.

The incident light power is calibrated before each measurement, using a calibrated quartz-windowed silicon solar cell (Newport) and a spectrometer (Ocean Optics) as described in previously report.[46] Incident photon-to-current efficiency (IPCE) measurements use a 300 W xenon arc lamp and a grating monochromator, equipped with filters to eliminate higher order diffractions. The light power of the xenon arc lamp is measured by an optical power meter (Newport 1918-C) and a UV-enhanced Si photodiode sensor.

The conductivity of each sample is measured using an electrical probe station (Signatone). Ohmic contacts to the hematite film are established by depositing a film of 5 nm titanium and 50 nm gold over the sample, through a shadow mask that contains an array of circular holes (1.25 mm in diameter). Electrical resistance between two nearest neighbor contacts is thus given by a standard two-probe *I–V* measurement. Multiple contact pairs are randomly selected and tested to give the mean resistance. Resistivity and conductivity for each sample are then calculated from the electrical flow channel geometry.

Acknowledgements

References

1 A. Fujishima and K. Honda, *Nature*, 1972, **238**, 37–38.

2 M. Gratzel, *Nature*, 2001, **414**, 338–344.

3 M. G. Walter, E. L. Warren, J. R. McKone, S. W. Boettcher, Q. Mi, E. A. Santori and N. S. Lewis, *Chem. Rev.*, 2010, **110**, 6446–6473.

4 K. Sivula, F. Le Formal and M. Gratzel, *ChemSusChem*, 2011, **4**, 432–449.

5 I. Cesar, K. Sivula, A. Kay, R. Zboril and M. Graetzel, *J. Phys. Chem. C*, 2009, **113**, 772–782.

6 A. G. Joly, J. R. Williams, S. A. Chambers, G. Xiong, W. P. Hess and D. M. Laman, *J. Appl. Phys.*, 2006, **99**, year.

7 L. A. Marusak, R. Messier and W. B. White, *J. Phys. Chem. Solids*, 1980, **41**, 981–984.

8 X. Y. Meng, G. W. Qin, S. Li, X. H. Wen, Y. P. Ren, W. L. Pei and L. Zuo, *Appl. Phys. Lett.*, 2011, **98**, 112104.

9 C. Toussaint, H. L. Le Tran, P. Colson, J. Dewalque, B. Vertruyen, B. Gilbert, N. D. Nguyen, R. Cloots and C. Henrist, *J. Phys. Chem. C*, 2014, **119**, 1642–1650.

10 J. A. Glasscock, P. R. F. Barnes, I. C. Plumb and N. Savvides, *J. Phys. Chem. C*, 2007, **111**, 16477–16488.

11 Y.-S. Hu, A. Kleiman-Shwarscstein, A. J. Forman, D. Hazen, J.-N. Park and E. W. McFarland, *Chem. Mater.*, 2008, **20**, 3803–3805.

12 J. S. Jang, J. Lee, H. Ye, F.-R. F. Fan and A. J. Bard, *J. Phys. Chem. C*, 2009, **113**, 6719–6724.

13 A. Kay, I. Cesar and M. Graetzel, *J. Am. Chem. Soc.*, 2006, **128**, 15714–15721.

14 A. Kleiman-Shwarscstein, Y.-S. Hu, A. J. Forman, G. D. Stucky and E. W. McFarland, *J. Phys. Chem. C*, 2008, **112**, 15900–15907.

15 S. Kumari, C. Tripathi, A. P. Singh, D. Chauhan, R. Shrivastav, S. Dass and V. R. Satsangi, *Curr. Sci.*, 2006, **91**, 1062–1064.

16 Y. Q. Liang, C. S. Enache and R. van de Krol, *Int. J. Photoenergy*, 2008.

17 C. J. Sartoretti, B. D. Alexander, R. Solarska, W. A. Rutkowska, J. Augustynski and R. Cerny, *J. Phys. Chem. B*, 2005, **109**, 13685–13692.

18 A. Annamalai, A. Subramanian, U. Kang, H. Park, S. H. Choi and J. S. Jang, *J. Phys. Chem. C*, 2015.

19 J. Deng, J. Zhong, A. Pu, D. Zhang, M. Li, X. Sun and S.-T. Lee, *J. Appl. Phys.*, 2012, **112**, year.

20 N. Mirbagheri, D. Wang, C. Peng, J. Wang, Q. Huang, C. Fan and E. E. Ferapontova, *ACS Catal.*, 2014, **4**, 2006–2015.

21 H. Tang, M. A. Matin, H. Wang, T. Deutsch, M. Al-Jassim, J. Turner and Y. Yan, *J. Appl. Phys.*, 2011, **110**, year.

22 G. Wang, Y. Ling, D. A. Wheeler, K. E. N. George, K. Horsley, C. Heske, J. Z. Zhang and Y. Li, *Nano Lett.*, 2011, **11**, 3503–3509.

23 N. T. Hahn and C. B. Mullins, *Chem. Mater.*, 2010, **22**, 6474–6482.

24 I. Cesar, A. Kay, J. A. G. Martinez and M. Gratzel, *J. Am. Chem. Soc.*, 2006, **128**, 4582–4583.

25 S. Kumari, A. P. Singh, Sonal, D. Deva, R. Shrivastav, S. Dass and V. R. Satsangi, *Int. J. Hydrogen Energy*, 2010, **35**, 3985–3990.

26 M. Grätzel, *J. Photochem. Photobiol., C*, 2003, **4**, 145–153.

27 C. Du, M. Zhang, J.-W. Jang, Y. Liu, G.-y. Liu and D. Wang, *J. Phys. Chem. C*, 2014.

28 Y. Lin, S. Zhou, S. W. Sheehan and D. Wang, *J. Am. Chem. Soc.*, 2011, **133**, 2398–2401.

29 X. Yang, R. Liu, C. Du, P. Dai, Z. Zheng and D. Wang, *ACS Appl. Mater. Interfaces*, 2014, **6**, 12005–12011.

30 O. Zandi, B. M. Klahr and T. W. Hamann, *Energy Environ. Sci.*, 2013, **6**, 634–642.

31 T. Atabaev, M. Ajmal, N. Hong, H.-K. Kim and Y.-H. Hwang, *Appl. Phys. A: Mater. Sci. Process.*, 2015, **118**, 1539–1542.

32 K. Ellmer, *J. Phys. D: Appl. Phys.*, 2000, **33**, R17–R32.

33 J. A. Glasscock, P. R. F. Barnes, I. C. Plumb, A. Bendavid and P. J. Martin, *Thin Solid Films*, 2008, **516**, 1716–1724.

34 S. Kment, Z. Hubicka, J. Krysa, D. Sekora, M. Zlamal, J. Olejnicek, M. Cada, P. Ksirova, Z. Remes, P. Schmuki, E. Schubert and R. Zboril, *Appl. Catal., B*, 2015, **165**, 344–350.

35 J. C. Slattery, K.-Y. Peng, A. M. Gadalla and N. Gadalla, *Ind. Eng. Chem. Res.*, 1995, **34**, 3405–3410.

36 D. K. Bora, A. Braun, S. Erat, O. Safonova, T. Graule and E. C. Constable, *Curr. Appl. Phys.*, 2012, **12**, 817–825.

37 J. Y. Kim, G. Magesh, D. H. Youn, J.-W. Jang, J. Kubota, K. Domen and J. S. Lee, *Sci. Rep.*, 2013, **3**, year.

38 Y. W. Phuan, M. N. Chong, T. Zhu, S.-T. Yong and E. S. Chan, *Mater. Res. Bull.*

39 H. C. Card and E. S. Yang, *IEEE Trans. Electron Devices*, 1977, **24**, 397–402.

40 C. H. Seager, *J. Appl. Phys.*, 1981, **52**, 3960–3968.

41 B. M. Klahr and T. W. Hamann, *J. Phys. Chem. C*, 2011, **115**, 8393–8399.

42 T. Lopes, L. Andrade, F. Le Formal, M. Gratzel, K. Sivula and A. Mendes, *Phys. Chem. Chem. Phys.*, 2014, **16**, 16515–16523.

43 F. L. Souza, K. P. Lopes, E. Longo and E. R. Leite, *Phys. Chem. Chem. Phys.*, 2009, **11**, 1215–1219.

44 J. Deng, X. Lv, J. Liu, H. Zhang, K. Nie, C. Hong, J. Wang, X. Sun, J. Zhong and S.-T. Lee, *ACS Nano*, 2015.

45 F. J. Morin and J. P. Maita, *Phys. Rev.*, 1954, **96**, 28–35.

46 M. Liu, C.-Y. Nam, C. T. Black, J. Kamcev and L. Zhang, *J. Phys. Chem. C*, 2013, **117**, 13396–13402.